



## Article

# Limb Temperature Observations in the Stratosphere and Mesosphere Derived from the OMPS Sensor

Pedro Da Costa Louro <sup>1,2,\*</sup>, Philippe Keckhut <sup>1</sup> , Alain Hauchecorne <sup>1</sup> , Mustapha Meftah <sup>1</sup> , Glen Jaross <sup>3</sup> and Antoine Mangin <sup>2</sup>

<sup>1</sup> Laboratoire Atmosphères, Observations Spatiales (LATMOS), Institut Pierre-Simon Laplace, Université Versailles-Saint Quentin, Université Paris-Saclay, 78280 Guyancourt, France; philippe.keckhut@latmos.ipsl.fr (P.K.); alain.hauchecorne@latmos.ipsl.fr (A.H.); mustapha.meftah@latmos.ipsl.fr (M.M.)

<sup>2</sup> ACRI-ST, 260 Route du Pin Montard, Sophia-Antipolis, 06130 Grasse, France; antoine.mangin@acri-st.fr

<sup>3</sup> NASA Goddard Space Flight Center, Greenbelt, MD 20771, USA; glen.jaross@nasa.gov

\* Correspondence: pedro.da-costa@latmos.ipsl.fr

**Abstract:** Molecular scattering (Rayleigh scattering) has been extensively used from the ground with lidars and from space to observe the limb, thereby deriving vertical temperature profiles between 30 and 80 km. In this study, we investigate how temperature can be measured using the new Ozone Mapping and Profiler Suite (OMPS) sensor, aboard the Suomi NPP and NOAA-21 satellites. The OMPS consists of three instruments whose main purpose is to study the composition of the stratosphere. One of these, the Limb Profiler (LP), measures the radiance of the limb of the middle atmosphere (stratosphere and mesosphere, 12 to 90 km altitude) at wavelengths from 290 to 1020 nm. This new data set has been used with a New Simplified Radiative Transfer Model (NSRTM) to derive temperature profiles with a vertical resolution of 1 km. To validate the method, the OMPS-derived temperature profiles were compared with data from four ground-based lidars and the ERA5 and MSIS models. The results show that OMPS and the lidars are in agreement within a range of about 5 K from 30 to 80 km. Comparisons with the models also show similar results, except for ERA5 beyond 50 km. We investigated various sources of bias, such as different attenuation sources, which can produce errors of up to 120 K in the UV range, instrumental errors around 0.8 K and noise problems of up to 150 K in the visible range for OMPS. This study also highlighted the interest in developing a new miniaturised instrument that could provide real-time observation of atmospheric vertical temperature profiles using a constellation of CubeSats with our NSRTM.

**Keywords:** temperature; Radiative Transfer; stratosphere; mesosphere; limb viewing; OMPS



**Citation:** Da Costa Louro, P.; Keckhut, P.; Hauchecorne, A.; Meftah, M.; Jaross, G.; Mangin, A. Limb Temperature Observations in the Stratosphere and Mesosphere Derived from the OMPS Sensor. *Remote Sens.* **2024**, *16*, 3878. <https://doi.org/10.3390/rs16203878>

Academic Editor: Carmine Serio

Received: 31 July 2024

Revised: 10 October 2024

Accepted: 15 October 2024

Published: 18 October 2024



**Copyright:** © 2024 by the authors. Licensee MDPI, Basel, Switzerland. This article is an open access article distributed under the terms and conditions of the Creative Commons Attribution (CC BY) license (<https://creativecommons.org/licenses/by/4.0/>).

## 1. Introduction

The middle atmosphere (MA) is a region that plays an important role in climate, acting as a link between the troposphere (0–15 km) and the thermosphere (>100 km). Emissions of particles and long-lived gases are mainly emitted in the lower atmosphere, whether from natural (volcanoes) or anthropogenic sources [1]. The upper atmosphere is mainly influenced by solar activity [2]. The MA is characterised by the presence of the ozone layer and dynamic processes on the different spatiotemporal scales that cross it [3]. In the long term, in addition to ozone chemistry, which is highly temperature dependent [4], the increase in greenhouse gases (GHGs) also leads to a cooling of the entire MA, which is associated with global warming at the surface [2,5–7]. While the stratosphere is strongly influenced by planetary waves and the associated stratospheric heating [8], the mesosphere is subject to the influence of gravity waves [9], which reverse the horizontal temperature gradient and lead to the generation of mesospheric inversions [10]. On the other hand, changes in the middle atmosphere have an impact on weather conditions [11–15] but

also on the highest layers of the thermosphere via space weather [16], which needs to be better quantified.

In recent years, the vertical domain of numerical weather models has been extended to higher altitudes and the spatial resolution has been improved [17–19]. However, the processes are difficult to model and validate due to the paucity of measurements, particularly in the mesosphere. Weather balloon soundings [20] and radio occultation observations using Global Navigation Satellite System (GNSS) signals from space [21] are limited to altitudes of about 30 km. Meteorological sounding rockets are no longer used because of their high cost [22]. Observations at nadir in the thermal infrared from space, such as the Stratospheric Sounder Unit (SSU) series, or in the microwave range, such as the Advanced Microwave Sounding Unit (AMSU) series on NOAA operational satellites, provide brightness temperatures below 45 km altitude and with extended vertical resolutions (about 5–10 km). However, these low-resolution satellite observations provide effective guidance for numerical weather prediction (NWP) models in the stratosphere. Observations from research sounders, such as those currently in use—MLS (Microwave Limb Sounder) onboard the AURA satellite or SABER (Sounding of the Atmosphere using Broadband Emission Radiometry) associated with the TIMED mission—cover the mesosphere with better resolution but sometimes with a strong bias [23]. Data from these satellites are not assimilated into the NWP models because they are used for research purposes. The absence of assimilated observations leads to biases and unrealistic variability in the European Centre’s meteorological analyses [24,25].

Solar occultation observations, such as the HALOE experiment onboard the UARS [26,27], allow temperature profiles to be obtained with a vertical resolution of the order of a kilometre. However, the observing geometry does not allow continuous observations. Molecular scattering can be used to derive temperature profiles in the middle atmosphere above 30 km in the absence of atmospheric particles. This technique has been successfully applied to Rayleigh lidar observations for over 40 years [28] at the Haute-Provence Observatory in France. It is also possible to obtain global temperature observations from space by looking at the illuminated limb using the onion-skin method. This method has been applied experimentally to several data sets obtained on different platforms, such as Solar Mesosphere Explorer [29]; WINDII on UARS [30]; OSIRIS on Odin [31]; and, more recently, GOMOS observations on ENVISAT [32]. These space experiments were not designed to provide temperature profiles and were in fact derived research products. These instruments were complex and allowed sophisticated observations of atmospheric composition [33]. GOMOS, for example, obtained precise height measurements by pointing at stars. Observations of molecular diffusion could probably be made with much simpler on-board systems that could be flown on cubesats [34]. These systems could then be deployed in constellations to provide operational, continuous observations unbiased by atmospheric tides. The recently launched OMPS (Ozone Mapping and Profiler Suite) instrument was not designed to measure temperature by molecular diffusion, as it was previously dedicated to atmospheric composition. However, it has a simpler instrument design than GOMOS, using a single image of the limb on a 2D sensor with no moving optics. Thus, it is interesting to evaluate the performance of this instrument, which is suitable for use on a future small platform such as those dedicated to the radiation budget [35]. The OMPS data have already been inverted to produce preliminary temperature profiles [36]. The analysis has been repeated here with our NSRTM to gain a better understanding of the sources of bias and to provide better temporal continuity of the series and improve the design of other future space systems.

Therefore, the objective of this study is to validate the method of inversion of limb observation data obtained with our NSRTM by comparing them with the long lidar series obtained within the framework of the NDACC [7]—and already validated on several occasions [23,37,38]—and with MSIS climatological models [39] or with ERA5 meteorological analyses [40] widely used by the scientific community. These comparisons will make it possible to highlight the strengths and weaknesses of the OMPS instrument design and our NSRTM in order to consolidate the design of smaller instruments for use in constellations.

Section 2 of this publication presents the OMPS observations, lidars from the NDACC network and the models used as a reference. Section 3 describes our NSRTM. Section 4 presents comparisons of the inverted OMPS data with the lidar and models data in conjunction with a variability estimation. Section 5 discusses the performance and improvements required for a reduced instrument with optimum performance. Finally, the conclusions of this study is presented in Section 6.

## 2. Description of the OMPS Instrument and Validation Data

### 2.1. OMPS Description

The Ozone Mapping and Profiler Suite (OMPS) consists of nadir-viewing and limb-viewing instruments onboard the Suomi NPP, NOAA-20 and NOAA-21 satellites, whose main objective is to study the composition of the stratosphere [41]. These satellites are in a sun-synchronous orbit at an altitude of about 830 km, and their position allows them to cover the entire globe ( $-90$  to  $90$  degrees latitude) 14.5 times a day (14.5 orbits). Because the instruments need to receive scattered sunlight to obtain high-quality observations, the data are selected as the satellite passes through the daytime portion of its orbit. The Limb Profiler (LP) instruments flown on Suomi NPP and NOAA-21 satellites measure the Earth's radiance in the 290–1020 nm spectral range, with sunlight as the main source scattered by atmospheric molecules (Rayleigh scattering) in our study area (30–85 km).

The operation of the LB is simple. The Earth's limb is observed through three slits with a fixed field of view of 1.85 degrees, covering an altitude range of 0.5 to 100.5 km. The first slit is centred on the satellite's orbit and the other two are oriented 4.25 degrees to the right and left of the first slit (250 km separation at the tangent point). After being scattered by the Earth's atmosphere, the light enters through one of the three slits. It then passes through a prism, which disperses the light. The spectral range studied is wide and the ultraviolet range is obtained with better resolution than in the visible and infrared. Then, these data are processed and corrected by the OMPS team to provide users with Level 1 data, where noise, linearity and calibration problems are eliminated. OMPS differs from the GOMOS instrument, which scanned the limb, in that it uses a CDD detector to simultaneously image the full vertical dimension of the atmosphere (Figure 1).

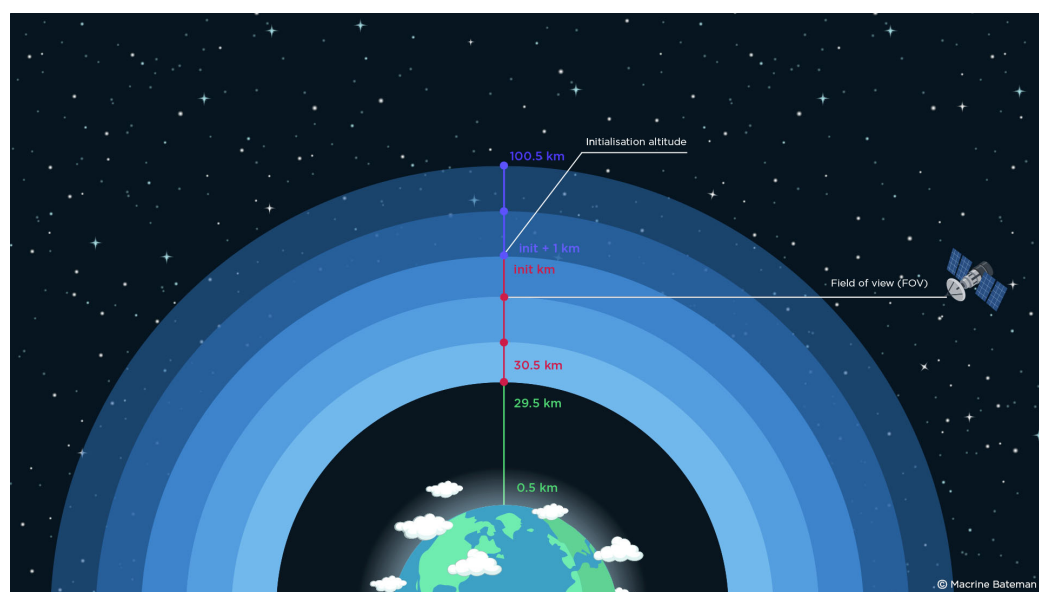


**Figure 1.** In our case, the green part of the profile is unused, the red part is the profile measured by OMPS and the violet part is simulated using an inverse exponential thanks to the red part. The initialisation altitude marks the ‘boundary’ between these 2 parts.

## 2.2. Description of Lidar Data

The Network for the Detection of Atmospheric Composition Change (NDACC) is an international network of ground-based remote sensing stations around the world with a number of objectives [42]. The main objective is to monitor changes in stratospheric ozone and the parameters and components that affect its chemical balance at a number of strategic points, and to derive changes and trends in atmospheric composition. It also aims to create a long-term database to validate the sensors in space. In the mesosphere, these reference data are severely lacking, making it difficult to estimate trends [2]. Lidar using molecular scattering is a well-suited technique to derive a vertical temperature profile in the middle atmosphere [28]. The instrument at the Haute-Provence Observatory has been used to validate a large number of instruments between 30 and 80 km altitude with 40 years of continuous measurements. These include missions such as UARS [26,27,37,38,43–46], ACE [47], MLS-Aura and SABER-TIMED [48,49]. These observations can also be used to ensure continuity and connectivity between similar sensors in space, such as the SSU/NOAA series [7] or AMSU/NOAA [50,51]. The quality of the NDACC lidar is ensured by continuous on-site intercomparison with a mobile instrument [23,37,38,52] and also by software intercomparison [53] or by using satellite observations as geographical transfers [54].

## 2.3. Description of the MSIS and ERA5 Reference Climatologies

MSIS is a climate model developed by the Naval Research Laboratory (NRL), which has recently been updated to version 2.0 [55]. It describes the mean behaviour of temperature, the density of numerous chemical species and mass density using an analytical formulation. In particular, it incorporates seasonal variations and fluctuations as a function of altitude, latitude and longitude. The main input data are the date in the year, the geographical coordinates and the altitude range used to obtain a vertical profile.

ERA5 is a hybrid analysis produced by the ECMWF (European Centre Medium for Weather Forecast). It is based on meteorological fields provided by a single meteorological model and constantly guided by various global observations covering the last 7 decades. This analysis provides estimates of numerous atmospheric climate variables for each day. The data used are resolved over 137 levels, from the surface to around 80 km [56].

MSIS and ERA5 operate differently. MSIS covers a wider vertical range from 0 to 1000 km, while ERA5 is limited to the mesopause with a so-called ‘sponge’ region in its upper part in the mesosphere. ERA5 provides a wealth of information about the atmosphere; however, here, we are only interested in temperature, pressure and density profiles. Comparisons already carried out show very good agreement between lidars and meteorological analyses in the stratosphere but major differences in the mesosphere [24,25].

## 3. Description of Our New Simplified Radiative Transfer Model (NSRTM)

### 3.1. Description of the Temperature Inversion Method

The inversion method based on molecular diffusion has been described in many previous works [28–32,36] and is based on the law of perfect gases linking temperature, atmospheric density and pressure, and the law of hydrostatic equilibrium linking density and pressure. This method has been widely used for lidar temperature measurements. The quality of these observations depends mainly on the amount of light collected. It should be remembered that the scattering signal observed at the limb from space decreases with altitude due to the decrease in molecular density. At a certain altitude, this signal becomes small compared to instrumental artefacts. One of the sources of uncertainty lies in the initialisation at the top of the profile; the estimation of the noise; and, therefore, the quantity of photons collected, which determines the accuracy of the measurements [57]. The part below 30 km is not used in the processing because it is potentially contaminated by ambient aerosols and particles [58]. In addition to inversion, measurements from space must take into account the fact that scattering occurs along the entire light path and that the line of sight passes through different atmospheric layers in different proportions. In order to assess the best spectral range, it is necessary to evaluate the impact of the different

components on the inversion according to the different wavelengths available through OMPS and to assess the quality of these corrections.

### 3.2. Initialisation Altitude, Stray Light and Background Correction Calculation

The NASA teams involved in processing the raw OMPS signals estimate only electronic noise, not other sources of noise or instrument error. Lidar analysis has shown us that these operations are extremely sensitive if even a weak signal remains in the altitude range where noise is estimated [57]. This is made even more critical in the case of the OMPS instrument by the fact that the altitude range is limited to 83.5 km, where molecular scattering may still be present in the signal at the highest altitudes. Therefore, the first step in the process is to define the altitude range for the inversion—in particular, the initialisation altitude (known as the init altitude). This is set at the point where the radiance measured at the upper level becomes greater than the radiance measured at the lower level. We consider that we are in the noise region when this happens and the init altitude is set to the lower altitude. We know from our experience with lidars and GOMOS that we have to correct for background noise, and from discussions with the NASA team we know that the instrument itself has problems with stray light due to the optical path. To estimate the stray light and background correction, we compare the signal from the MSIS model with the observations. We simulate a radiance profile from the MSIS density profile. We calculate a constant signal to remove or add to the signal to obtain the same slope in the simulated MSIS and OMPS radiance profiles in the last 5 km.

Thus, the stray light level is estimated using the formula given below:

$$\text{Bruit} = \frac{\text{profil}_{\text{init}-5} \times \text{RadMSIS}_{\text{init}} - \text{profil}_{\text{init}} \times \text{RadMSIS}_{\text{init}-5}}{\text{RadMSIS}_{\text{init}-5} - \text{RadMSIS}_{\text{init}}} \quad (1)$$

This new stray light and background correction is more or less effective depending on the wavelength range. In the visible range, in particular, residual scattering must be estimated; otherwise, significant differences of up to around 150 K can be observed above 70 km (Figure 2).

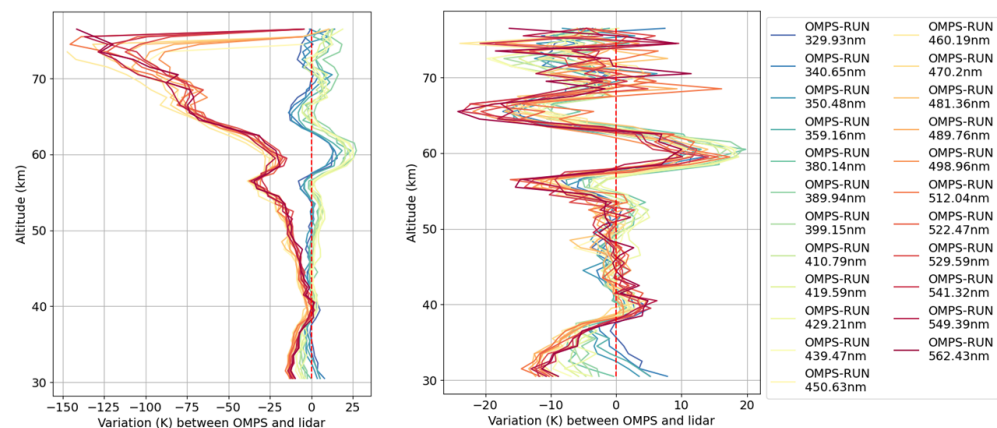


**Figure 2.** Example of the effect of noise correction on a daily profile in relation to the position of the site on La Réunion where the lidar is located. Temperature inversions are performed using several wavelength bands available on the OMPS instrument. On the left are the profiles with noise estimated from the latest channels. On the right are the profiles with noise estimated using the MSIS model as described in Section 2.

### 3.3. Onion Peel Method

As mentioned above, the OMPS team provides an integrated radiance profile with 1 km vertical resolution, i.e., the radiance measured on the line of sight is affected by the upper layers. In order to correct for the contribution of the other layers, we apply the



so-called ‘onion peel’ technique, which allows us to obtain the radiance value of each layer by ‘removing’ the layers above it:

$$\text{newprofil}_i = \text{profil}_i - \text{profil}_i \times \left( \sqrt{j+1-j} - \sqrt{j-i} \right)$$

with  $j = i + 1$

$(\sqrt{j+1-j} - \sqrt{j-i})$  represents the weight of layers  $j$  in layer  $i$ , proportional to the length of the line of sight  $i$  in the  $j$  layer.

This method assumes that the atmospheric layers are homogeneous over the viewing distance. It gives excellent vertical resolution (of the order of a km) but does not provide information on horizontal variability better than a few 100 km as a function of altitude (Figure 3).

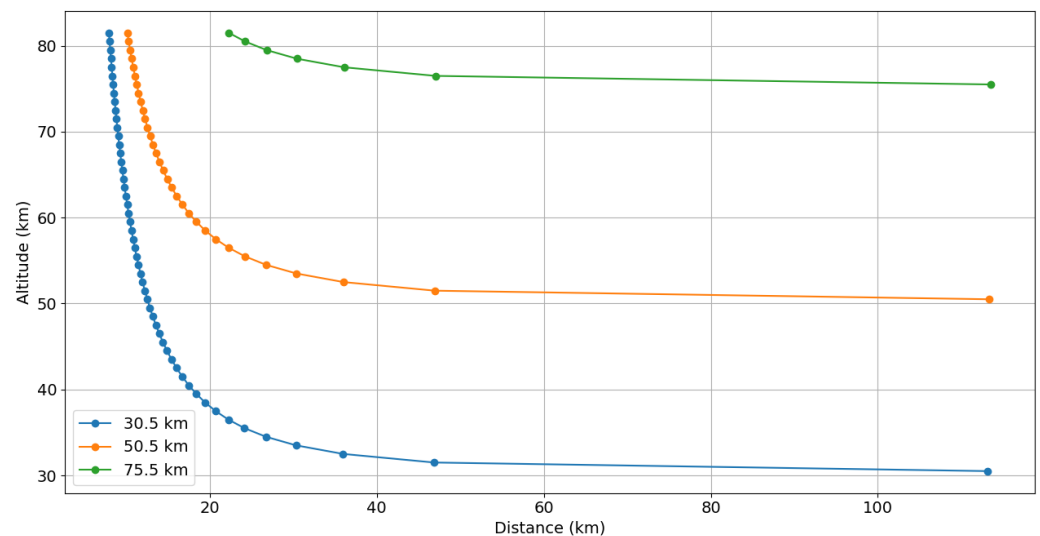


**Figure 3.** Representation of the horizontal resolution for three tangent heights, each point represents a layer measured by OMPS. As an example with the blue curve, the first point at 113 km represents the distance observed by OMPS between the layer observed, here 30.5 km, and the next layer 31.5 km; the second point at 43 km still represents the distance observed by OMPS at 30.5 km but this time between the layers 31.5 and 32.5 km; and so on.

### 3.4. Observation Geometry for OMPS Layers

Sunlight entering the instrument is attenuated by the absorption of atmospheric constituents. In the UV/Visible spectral range, it is mainly  $O_3$  and  $NO_2$  that cause a reduction in the radiance of the observed layers, particularly around areas where the constituent is highly concentrated—in our case, the stratosphere. Similarly, molecular scattering (known as Rayleigh scattering) causes photons to be scattered by the molecules encountered, reducing the signal received, particularly towards the lowest layers where the density of the air increases. Therefore, it is necessary to evaluate the distance of each path in order to apply a reduction corresponding to the concentration of the component in the layer under consideration.

$$D_{c-Sati} = \sqrt{R_{couche_i}^2 - R_{couche_{i-1}}^2} \quad (2)$$

$D_{c-Sati}$  corresponds to the distance covered in layer  $i$  by the radiance to reach the satellite.

$R_{couche_i}$  corresponds to the terrestrial radius at layer  $i$ .

By performing the calculation for the top layer, it is possible to estimate the signal attenuation for the layer below and thus obtain the calculation for the entire vertical profile. This method assumes that the layers are homogeneous in composition (Figure 4).

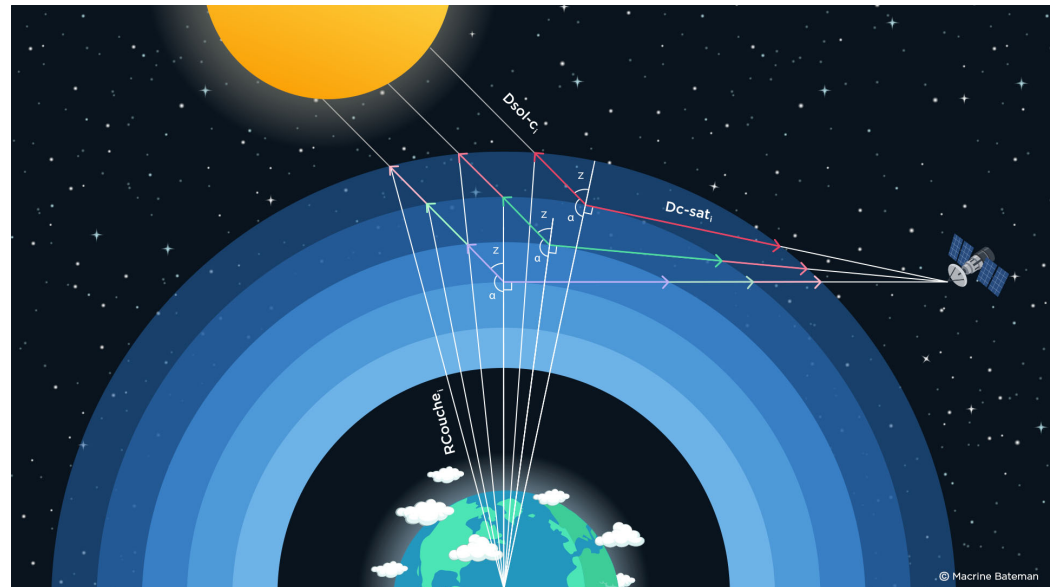


**Figure 4.** This diagram illustrates the path taken by the radiance in each layer observed by OMPS. At each layer, the radiance is scattered by air molecules and absorbed by ozone and nitrogen dioxide molecules.  $R_{Couche_i}$  represents the radius from the Earth to the given layer, and  $D_{c-sat_i}$  represents the distance that the radiance in layer  $i$  crosses to reach the satellite. Similarly,  $D_{sol-c_i}$  represents the distance travelled by the radiance arriving from the sun to the layer.

Once the distance matrix is obtained, and using modelled density profiles, modelled  $\text{NO}_2$  profiles and  $\text{O}_3$  profile measurements, we can measure the total radiance loss that applies to each observation path. The first thing we notice is that between 45 km and 30 km, the total correction to be applied to the profile to correct for this is almost multiplied by 10, whatever the wavelength (Figure 5).

Next is the wavelength correction difference. From around 330 nm to 420 nm, the total attenuation of the signal decreases to a minimum as we leave the Huggins absorption band for  $\text{O}_3$  and the Rayleigh scattering also decreases. From 420 nm, despite the fact that the Rayleigh scattering continues to decrease, we see an increase in the total attenuation of the signal. This is due to the fact that we enter the Chappuis absorption band for  $\text{O}_3$ . The  $\text{NO}_2$  correction remains more or less constant throughout the spectrum of the study, with a slight increase up to around 400 nm and then a slight constant decrease. Again, depending on the wavelengths chosen, the total correction required for the profile is almost multiplied by 10 when taken on the same layer (Figure 5).

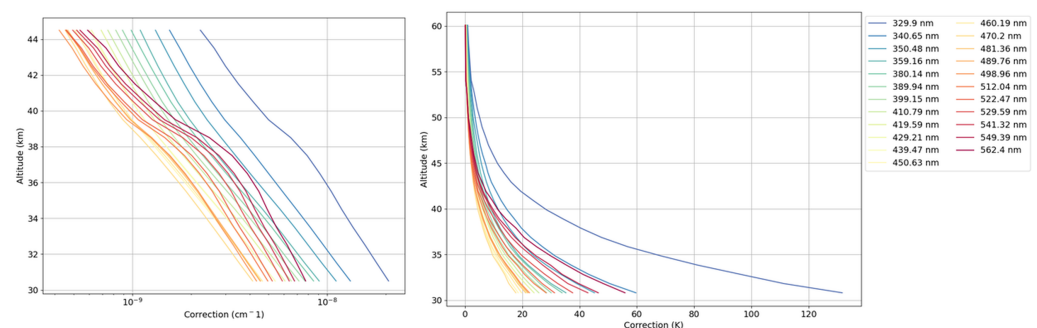


**Figure 5.** The left figure shows the correction applied to the radiance profile per cm at different wavelengths, while the right figure shows the effect of this correction in kelvin on the temperature profiles at the same wavelengths.

### 3.5. Diffusion and Absorption of the Various Constituents of the Middle Atmosphere

#### 3.5.1. Rayleigh Scattering

Since our initial hypothesis assumes Rayleigh scattering of the atmosphere above 30 km, we can use the molar mass of the air to find the number of ‘Rayleigh’ ( $N_{i\text{-Rayleigh}}$ ) molecules in each layer of the atmosphere:

$$N_{i\text{-Rayleigh}} = \frac{\rho_i \times N_A}{M_{\text{air}}} \quad (3)$$

where

$\rho_i$  is the density of the layer in  $\text{cm}^{-3}$ ;

$N_A = 6.022 \times 10^{23} \text{ mol}^{-1}$  Avogadro’s number;

$M_{\text{air}} = 28.965 \text{ g/mol}$  the molar mass of air.

The Rayleigh scattering per molecule is given by the formula below [59]:

$$\sigma_{\lambda\text{-Rayleigh}} = \frac{24 \times \pi^3 \times (n_s^2 - 1)^2}{\lambda^4 \times N_s^2 \times (n_s^2 + 2)^2} \times \frac{6 + 3 \times \rho_n}{6 - 7 \times \rho_n} \quad (4)$$

where  $\sigma_{\lambda\text{-Rayleigh}}$  is the wavelength in  $\text{cm}$   $\lambda$ ;

$n_s$  is the refractive index of the air at  $\lambda$  (unitless);

$N_s$  is the numerical molecular density of air;

$\rho_n$  is the depolarising factor at  $\lambda$  (unitless).

$\sigma_{\lambda\text{-Rayleigh}}$  and  $N_{i\text{-Rayleigh}}$  allow us to find the total Rayleigh scattering of a layer:

$$\beta_{\lambda i\text{-Rayleigh}} = \sigma_{\lambda\text{-Rayleigh}} \times N_{i\text{-Rayleigh}} \quad (5)$$

From around 330 to 380 nm, the Rayleigh correction’s contribution to total signal attenuation increases to almost 100%; at these wavelengths, it is the greatest source of error. After 380 nm, its share gradually decreases, giving way to  $\text{O}_3$  and  $\text{NO}_2$  absorption (Figure 6).

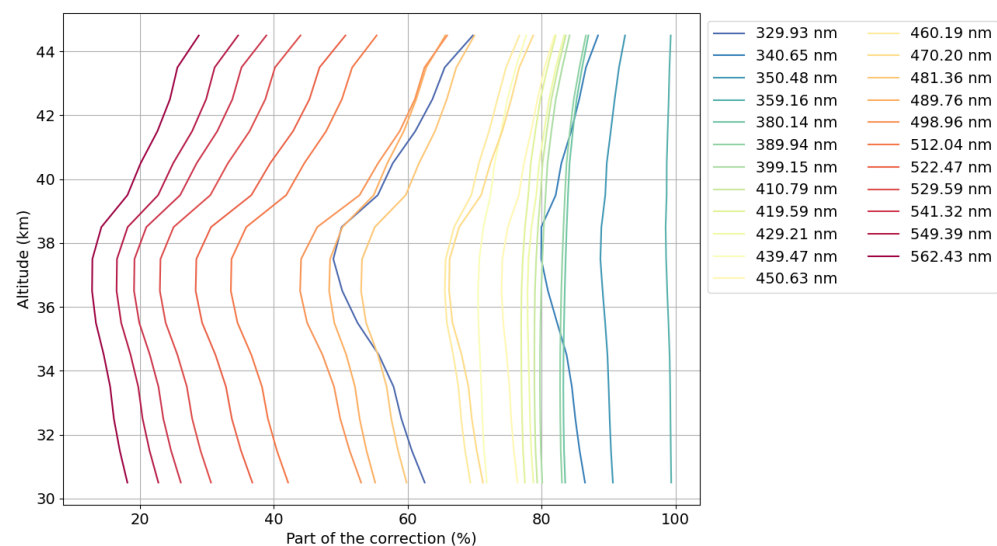


**Figure 6.** Share of Rayleigh scattering in total signal attenuation in % at different wavelengths. This figure should be read in conjunction with Figures 5, 8 and 10 and provides a better understanding of the roles of Rayleigh scattering and  $\text{O}_3$  and  $\text{NO}_2$  absorption in the corrections applied to the radiance profile and, by extension, to the temperature profiles.

#### 3.5.2. Ozone Absorption

$\text{O}_3$  absorption is measured in the laboratory for a given wavelength and temperature ( $\sigma_{\lambda\text{-O}_3}$ ) [60]. The number of  $\text{O}_3$  molecules is measured by the same instrument that measures



OMPS radiance profiles [61] (Figure 7). With these two values, we obtain the ozone absorption for each layer measured by OMPS:

$$\beta_{\lambda\text{-O}_3} = \sigma_{\lambda\text{-O}_3} \times N_{\text{i-O}_3} \quad (6)$$

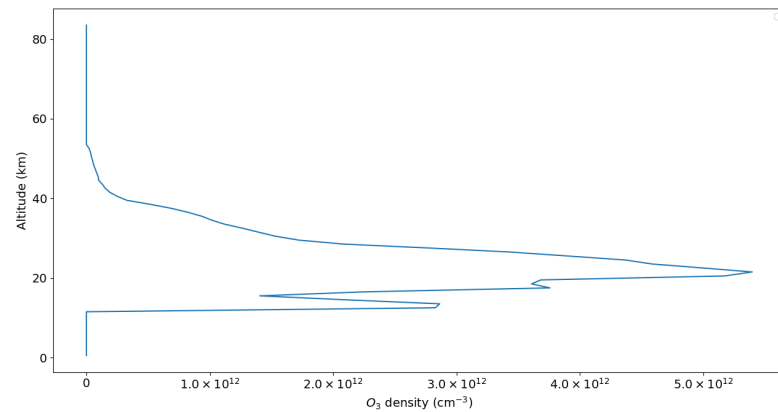


**Figure 7.** Example of an O<sub>3</sub> profile measured by OMPS in the middle atmosphere.

The effect of O<sub>3</sub> on the correction begins to be felt as the ozone concentration begins to increase (Figure 7), the effects of the Huggins–Chappuis absorption bands can be seen in the total attenuation of the signal. In the Huggins absorption band, the O<sub>3</sub> absorption accounts for a large part of the correction (up to 40%), but as Rayleigh scattering is also very strong at these wavelengths, it is not the most important part of the correction. Then, between the two absorption bands, the proportion decreases to almost 0%. Once the start of the Chappuis band is reached, it increases again until it reaches 80% and becomes the largest source of error. It should be noted that the Huggins and Chappuis bands are very similar in absorption values, the difference being that Rayleigh scattering is much weaker in the Chappuis band (Figure 8). The final point to note, which is taken into account in our NSRTM, is the consideration of variations in O<sub>3</sub> absorption as a function of temperature. For example, around 350 nm, we have a 16% drop in O<sub>3</sub> absorption for every 10 K loss.

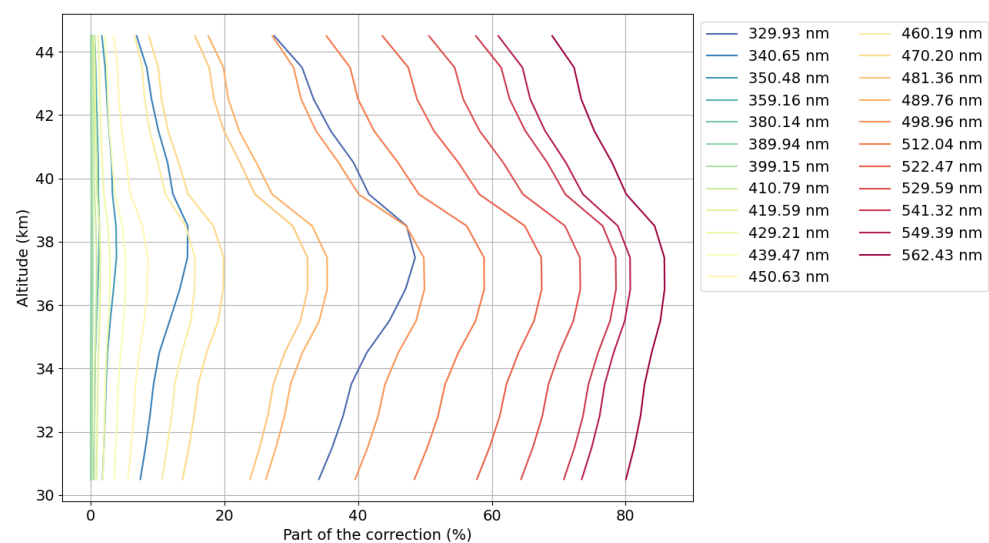


**Figure 8.** Share of O<sub>3</sub> absorption in total signal attenuation in % at different wavelengths.

### 3.5.3. Nitrogen Dioxide Absorption

NO<sub>2</sub> absorption is also measured in the laboratory for a given wavelength and temperature ( $\sigma_{\lambda\text{-NO}_2}$ ) [62]. Variations in NO<sub>2</sub> concentration are given by the WACCM model (Whole

Atmosphere Community Climate Model [63]), which is a climate modelling software package developed to study and simulate the complex large-scale interactions between different components of the Earth's atmosphere. The profiles given are monthly profiles. These two values give the absorption of Nitrogen Dioxide for each layer modelled by WACCM (Figure 9):

$$\beta_{\lambda_{\text{Ti-NO}_2}} = \sigma_{\lambda_{\text{T-NO}_2}} \times N_{\text{i-NO}_2} \quad (7)$$

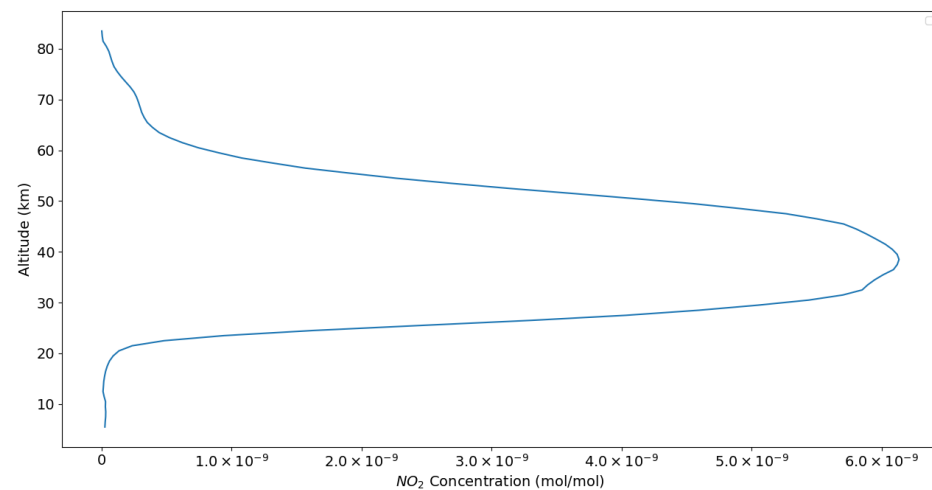


**Figure 9.** Example of a NO<sub>2</sub> profile in the middle atmosphere. WACCM gives an average profile per month for each year.

As with O<sub>3</sub>, the effect of correcting for NO<sub>2</sub> begins when its concentration in the atmosphere starts to rise (Figure 9). NO<sub>2</sub> absorption varies little compared with O<sub>3</sub> absorption and Rayleigh scattering in our study area, so the main cause of variation in its share of total signal attenuation comes from the variation in O<sub>3</sub> absorption and Rayleigh scattering (Figure 10).

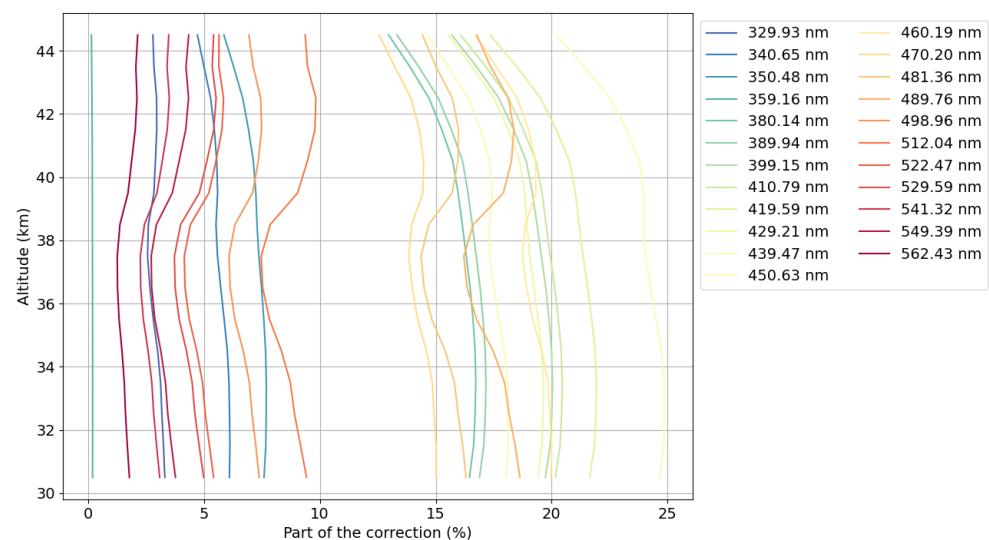


**Figure 10.** Share of NO<sub>2</sub> absorption in total signal attenuation in % at different wavelengths.

### 3.6. Correcting the Attenuation of Radiance Profiles

The total attenuation of the sign, as seen in Section 3.4, coupled with the light paths calculated in Section 3.3, enables the radiance profile to be corrected:

$$\text{newprofil2}_i = \text{newprofil}_i \times e^{D_{\text{c-sat}_i} \times (\beta_{\lambda_i\text{-Rayleigh}} + \beta_{\lambda_{\text{T-O}_3}} + \beta_{\lambda_{\text{T-NO}_2}})} \quad (8)$$

Now that we have corrected for the loss of radiance caused by Rayleigh scattering, O<sub>3</sub> and NO<sub>2</sub> absorption during the layer-to-satellite ‘path’, we need to correct for the same loss caused during the sun-to-layer ‘path’. First, we calculate the Rayleigh phase function at our scattering angle:

$$P_{\text{ray}\theta} = \frac{3}{4(1+2\gamma)} \left[ (1+3\gamma) + (1-\gamma) \cos^2 \theta \right] \quad (9)$$

where

$$\gamma = \frac{\rho_n}{2 - \rho_n} \quad (10)$$

$$\theta = \hat{z} + 90^\circ \quad (11)$$

$\hat{z}$  is the measured zenith angle.

We then calculate the angular volume diffusion coefficient:

$$\beta_{\theta\lambda_i} = \frac{\beta_{\lambda_i\text{-Rayleigh}}}{4\pi} \times P_{\text{ray}\theta} \quad (12)$$

The new radiance profile is as follows:

$$\text{newprofil3}_i = \frac{\text{newprofil2}_{2i}}{\beta_{\theta\lambda_i}} \quad (13)$$

(Note that variations in the zenith angle are negligible, so we will keep the  $z$  measured throughout the profile).

As with the layer–satellite ‘path’, the sun–layer ‘path’ also generates radiance losses caused by the combination of the observation geometry and Rayleigh scattering, O<sub>3</sub> and NO<sub>2</sub> absorption. According to al-Kashi’s theorem, we can write

$$D_{\text{c-soli}}^2 - 2 \times R_{\text{couche}_i} \times \cos \alpha \times D_{\text{c-soli}} + R_{\text{couche}_i}^2 - R_{\text{couche}_{i+1}}^2 = 0 \quad (14)$$

with

$$\alpha = 180^\circ - z \quad (15)$$

As with the layer–satellite path, this matrix continues until the last layer where the treatment is applied, allowing the profile to be corrected.

$$\text{newprofil4}_i = \text{newprofil3}_i \times e^{D_{\text{sol-c}_i} \times (\beta_{\lambda_i\text{-Rayleigh}} + \beta_{\lambda_{\text{T-O}_3}} + \beta_{\lambda_{\text{T-NO}_2}})} \quad (16)$$

newprofil4 and newprofil3 are the radiance profiles received by each layer, but we want the radiance profile that should have been measured by the satellite; so, we need to make this last calculation:

$$\text{newprofil5}_i = (\text{newprofil4}_i - \text{newprofil3}_i) \times \beta_{\theta\lambda_i} \quad (17)$$

Calculating these two paths gives us the horizontal resolution of the instrument. This resolution changes with altitude but always reaches a maximum at around 110 km, as shown in Figure 3.

This resolution, combined with the effects of Rayleigh scattering and O<sub>3</sub> and NO<sub>2</sub> absorption, results in a variation in the radiance profile obtained that must be corrected; this correction has a direct effect on the temperature profile, as shown in Figure 11.

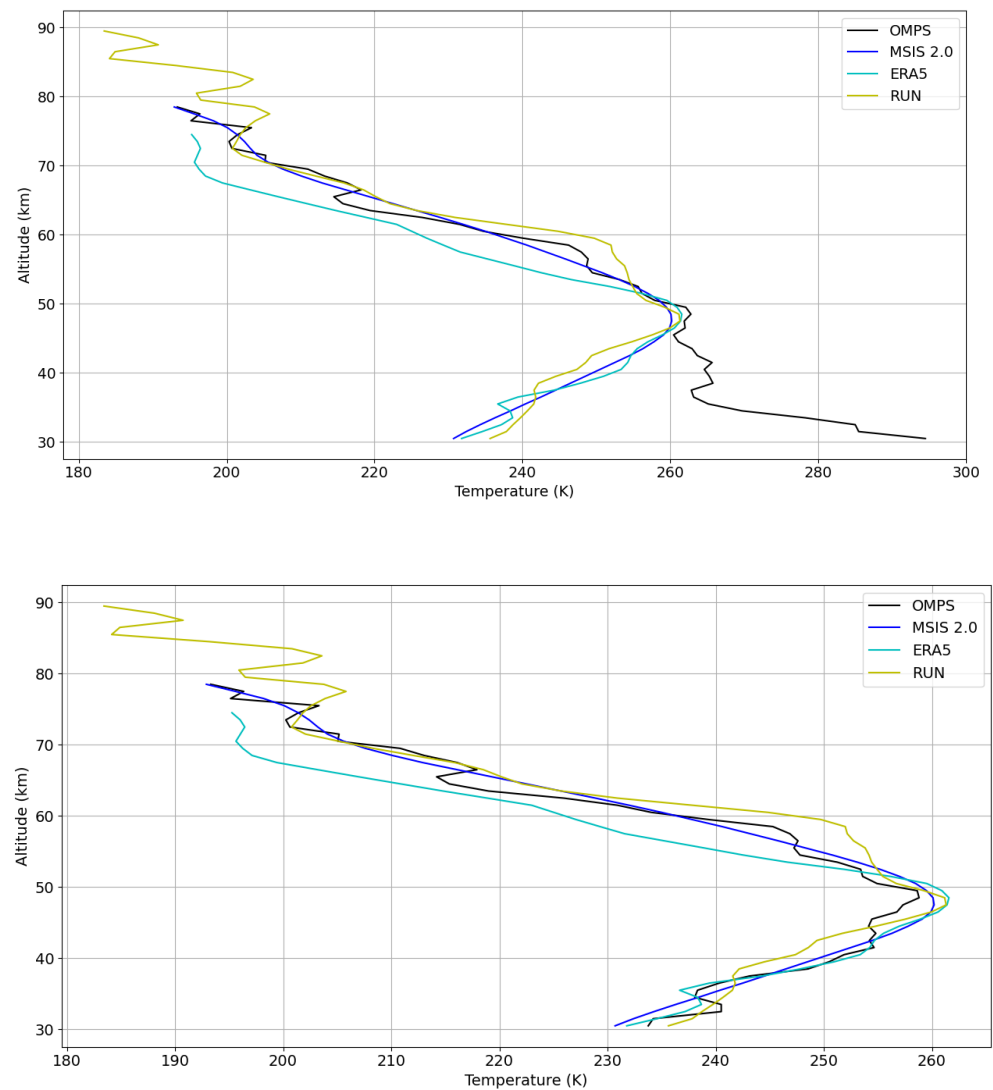


**Figure 11.** The upper figure shows a temperature profile obtained by OMPS without correction of the radiance profile; the lower figure is the same temperature profile but with correction of the radiance profile by our NSRTM. The temperature profiles of the ERA 5 and MSIS 2.0 models and the lidar profile (in this case, the Réunion lidar) obtained on the same day show the extent of the correction.

### 3.7. Calculating the Temperature Profile

Now that we have the corrected radiance profile, and given that Rayleigh scattering is proportional to atmospheric density in our study space, we can calculate the temperature profile of the radiance profile by applying the law of perfect gases, hydrostatics and an initialisation temperature:

$$h_{scale} = \frac{0.287 \times temp_{init}}{Gz_{init}} \quad (18)$$

Initialisation pressure:

$$P_{init} = newprofil5_{init} \times h_{scale} \times Gz_{init} \quad (19)$$

Calculating the pressure and temperature profiles:

$$P_i = P_{i+1} + \frac{newprofil5_i + newprofil5_{(i+1)}}{2} \times Gz_i \quad (20)$$

$$T_i = \frac{P_i \times 0.287}{\text{newprofil5}_i} \quad (21)$$

where

$\text{temp}_{\text{init}}$  is the MSIS 2.0 model temperature at initialisation altitude;

$G_{z_{\text{init}}}$  is gravity at the initialisation point.

#### 4. Comparisons of Temperature Profiles Obtained with the OMPS Instrument with Lidars from the NDACC Network

##### 4.1. Collocation Information

The lidars chosen for the comparisons are sites with different characteristics and high-performance instruments that have already been extensively involved in numerous instrumental comparisons:

- Observatoire de Haute-Provence (OHP) located in the south of France at 43.94°N, 5.71°E;
- Mauna Loa Observatory (MLO) located in Hawaii at 19.54°N, 155.58°W;
- Observatoire de Physique Atmosphérique de La Réunion (RUN) located in the Indian Ocean on the island of Réunion at the geographical position 21.1°S, 55.4°E;
- Hohenpeißenberg Meteorological Observatory (HOH) located in Germany at 47.80°N, 11.02°E.

In order to ensure a good match between the lidar positions and the OMPS satellite data, we chose a 10° \* 10° geographical area centred on the lidar positions. The chosen geographical area is a compromise that allows us to retrieve one satellite data point per day, thus allowing us to base the comparison on a larger number of cases. It should be noted that in order to obtain high-quality temperature profiles, the observations must be made at night and in cloudless weather conditions. Also, for reasons of cost and operator availability at night, the lidars do not operate continuously and we do not have a reference temperature profile every day. To complete the comparisons between OMPS and lidar observations, we performed a systematic comparison with the MSIS 2.0 and ERA5 models. The temperature profiles of the models were extrapolated to the position of the lidars and the time of OMPS passage.

##### 4.2. Wavelength Analysis

We have analysed the different temperature profile inversions obtained for the different wavelengths available with the OMPS spectrometer, with steps of 1 nm, over the spectral range from 330 to 562 nm. The received signal is a combination of the scattering efficiency of solar radiation and attenuation. The solar spectrum follows Planck's law [64] with a maximum around 550 nm. In our study region, between 230 and 1020 nm, the power per square metre received by the atmosphere can vary by up to a factor of four depending on the wavelength chosen. Molecular scattering efficiency depends on Rayleigh's law [59] and gives a maximum scattering efficiency for short wavelengths; in our study range, scattering varies by up to a factor of 100. As described in previous chapters, the total attenuation due to atmospheric composition modulates the signal by a factor of 10 and must also be taken into account. It appears that the wavelength range around 450 nm is ideal, but for wavelengths shorter than 330 nm, the conditions for obtaining good temperature profiles are no longer met due to attenuation (Figure 12).



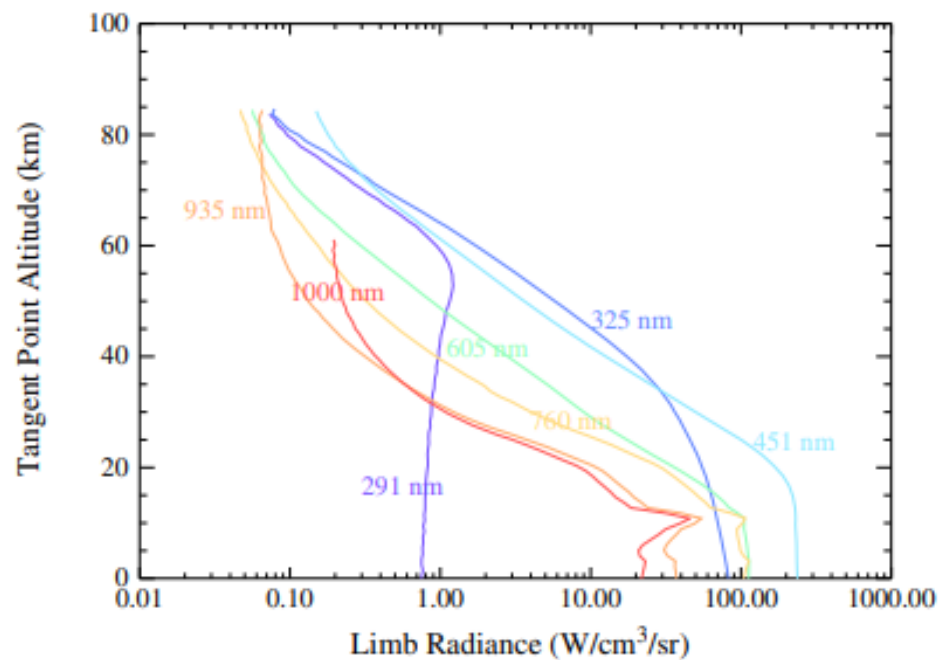


**Figure 12.** Example of Earth limb radiances measured by OMPS on 13 August 2012 at 45°N latitude [41].

Since scattering is optimal at short wavelengths, we stopped this sensitivity study at 562 nm. On the other hand, due to instrumental problems, the spectral range between 360 and 380 nm is not available. For reference, we performed this analysis on four lidar sites for 2015. In particular, we observed similar behaviour for the comparison with all four sites. The differences are radically different for wavelengths between 399.15 and 450.63 in the mesosphere between 50 and 70 km, as can be seen, for example, for the Réunion site (Figure 13).

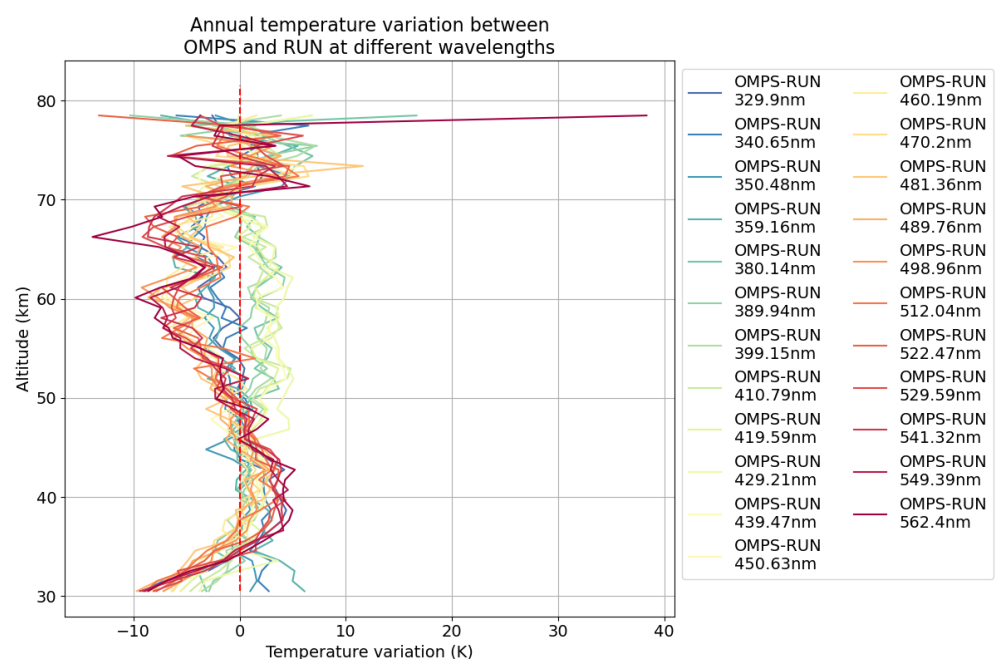


**Figure 13.** Annual temperature difference between OMPS and the lidar on Réunion Island at different wavelengths.

The comparisons show two groups of wavelengths, one showing positive temperature variations (1–3 K) for wavelengths between 380 and 439 nm and the other showing negative differences for short (<359 nm) and long (>450 nm) wavelengths, with the results also differing slightly between long and short wavelengths. After analysing other results from the NASA team, it appears that the effect is due to stray light on one of the channels. This effect may be due to the design of the instrument itself. To keep things simple, there are three fundamentally different regimes in OMPS to correct for the stray light error: <360 nm, 375–450 nm and >450 nm. These three regimes correspond to the three groups mentioned earlier (Figure 14).

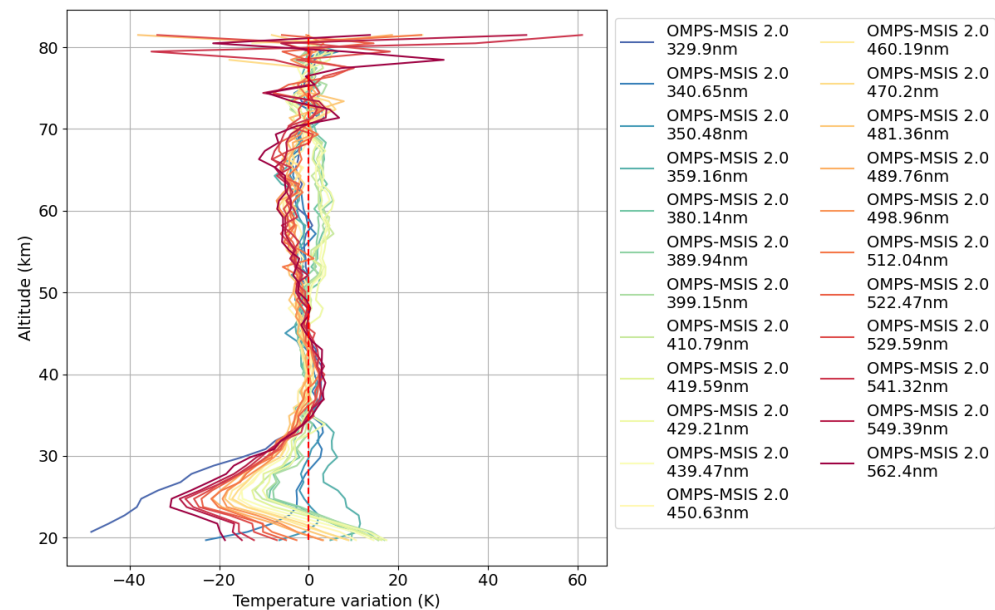


**Figure 14.** Annual temperature difference between OMPS and the MSIS 2.0 model at different wavelengths. The effect of aerosols on temperature profiles can be seen between 20 and 30 km. As the wavelength increases, aerosol scattering takes precedence over molecular scattering. Lidars do not provide temperature data below 30 km, so we show this phenomenon using MSIS differences.

Analysis at lower altitudes towards the middle stratosphere shows discrepancies, probably due to the presence of aerosols. The comparison with lidars, which are also sensitive to the presence of aerosols, is not relevant for the validation of the OMPS inversions in this altitude range. On the other hand, the comparison with the MSIS climatological model shows that the differences logically increase with wavelength, confirming the reason for these differences. As this contribution is difficult to correct, it seems more appropriate to select short wavelengths, thereby minimising this effect. Also, as we have shown in Section 3.2, Figure 2, the shortest wavelengths are least affected by noise in the upper mesosphere. For all these reasons, we have chosen to select wavelengths between 335 and 345 nm for this study and to add them together to reduce the measurement noise due to the entire acquisition chain, from optics to detector.

The standard deviation between these different profiles, calculated for each wavelength, allows us to estimate the intrinsic error associated with our inversion method applied to the OMPS observations. In a perfect case, all the wavelengths should give the same results, since they are all looking at the same scene. Therefore, the temperature variations between the signals from the different wavelengths are due to the uncertainty in the radiance measurement. The corresponding error is less than 1 K (Figure 15).

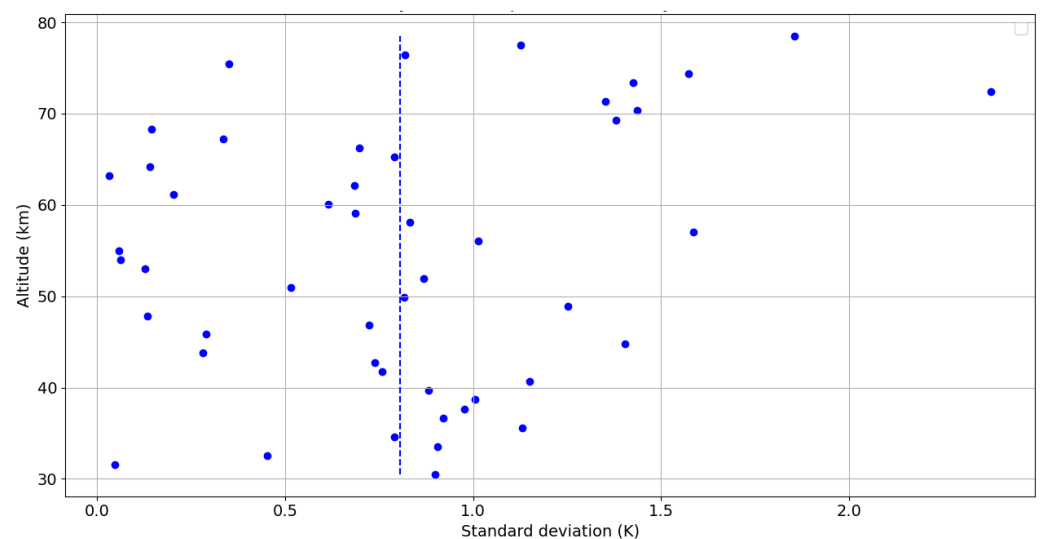


**Figure 15.** Scatterplot and mean standard deviation of the temperature inversion method with OMPS obtained with each wavelength as a function of altitude.

#### 4.3. Results of Temperature Analyses for Each Site

As mentioned in Section 4.1, we compared the results obtained by OMPS with four lidars from the NDACC network and the two models MSIS and ERA5. Below is the list of the number of comparisons for each position:

- OHP: 1685 comparisons for MLS, MSIS and ERA5, and 777 comparisons against lidar between 2015 and 2020.
- MLO: 990 comparisons for MLS, MSIS and ERA5, and 493 comparisons with lidar between 2015 and July 2018.
- RUN: 1207 comparisons for MLS, MSIS and ERA5, and 257 comparisons against lidar between 2015 and 2020, there are no comparisons for the year 2016.
- HOH: 597 comparisons for MLS, MSIS and ERA5, and 263 comparisons against lidar for the 2 years 2015 and 2016.

The temperature differences between OMPS, MSIS, ERA5 and the lidars show very similar results, never exceeding 5 K, except for the HOH lidar at high altitude and the MLO lidar below 35 km. For the HOH lidar, this is probably due to the fact that the statistical error associated with this lidar is smaller than that of the other lidars and that its range rarely exceeds 75 km. At this altitude, the temperature error of the lidar exceeds 20 K, so the results for this high-altitude site should be treated with caution. For the MLO lidar, we believe that the effect of aerosols, which we have not taken into account, is responsible for this variation. In fact, we observe a slight increase in the standard variation compared to all lidars below 35 km, and it is known that stratospheric aerosols begin to be observed at these altitudes [58]. Therefore, this altitude range is subject to uncertainties—although, in view of the proportions and results available to us, this uncertainty remains more or less small depending on the sites (Figure 16).

The models behave differently. First of all, between 30 and 50 km, the models show similar results to the lidars in terms of temperature variation, but it is in the standard deviation that we can see the differences. We can see that at almost all sites the standard deviation of ERA5 is lower than that of MSIS, which is generally close to or slightly higher than that of the lidar. Here, we can see the difference between an analytical model (MSIS) and a model that assimilates real data (ERA5). After 50 km, the results for ERA5 start to change: the temperature difference increases sharply to a maximum of 10 K difference, and there is also a sharp increase in its standard deviation, which joins the lidar and MSIS values. It is important to note that significant biases were already observed above 50 km

for ERA5 compared to the lidars [25]. Comparisons with MSIS remain stable even after 50 km (Figure 16).

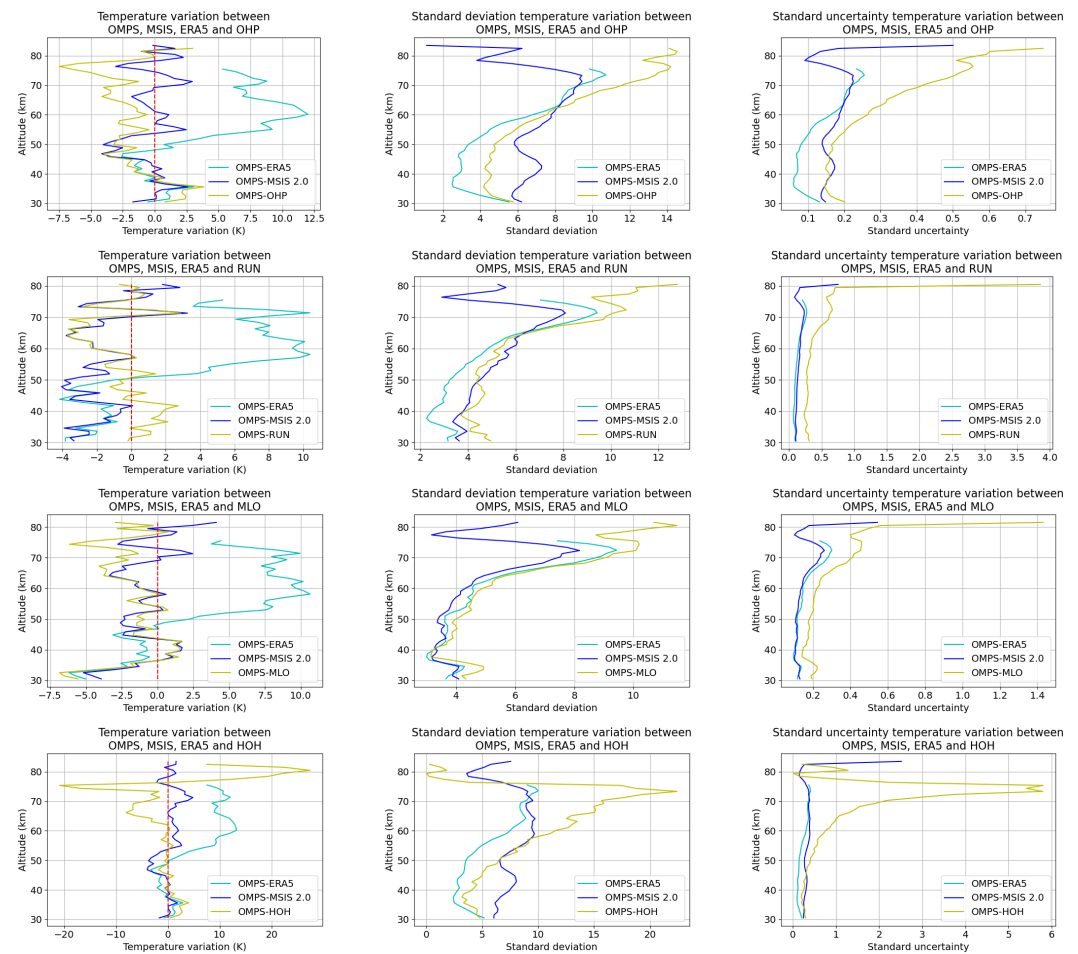


**Figure 16.** Comparisons of OMPS temperature profiles with ERA5, MSIS 2.0 and HOH. On the left are the differences between OMPS and the various sources compared; in the centre the standard deviation; and on the right the uncertainty on the standard deviation. In order from first to last line, the study sites are OHP, RUN, MLO and HOH.

At higher altitudes, the standard deviation gradually increases in the mesosphere due to gravity waves and instrumental errors in the lidar and OMPS signals. The systematic deviations observed in the mesosphere may be induced by atmospheric tides, since the measurements are not made simultaneously. We note that for HOH and OHP, the standard deviation drops suddenly at very high altitudes. This is only due to the fact that the temperature profiles of these lidars generally stop earlier than those of MLO and RUN, so there are very few values to compare at very high altitudes and the standard deviation is, therefore, not significant. As can be seen, the uncertainty in these standard deviations is very small, except for the last kilometre where there is a sharp increase. The reason for this is that at this altitude there are far fewer comparisons due to the variable initialisation altitude. It is important to understand that these variations are not ‘errors’ but rather expected results, as illustrated in Figure 17:

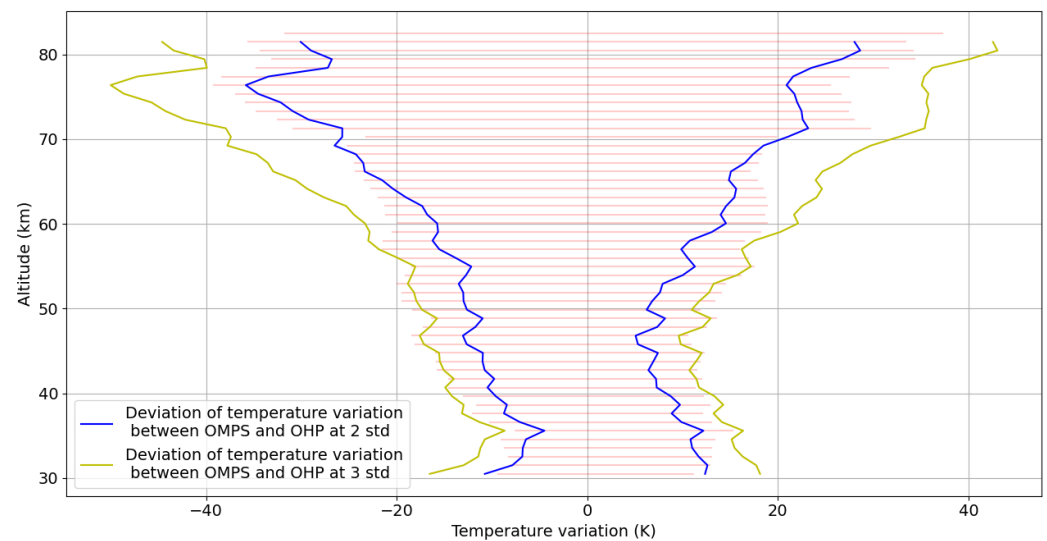


**Figure 17.** Deviation in temperature between OMPS and OHP. The red zone represents the calculated expected differences. The blue and yellow curves represent the temperature differences between OMPS and OHP at 2 and 3 stds.

Using an internal procedure, we can calculate the variations due to gravity waves, atmospheric tides and errors in the measurements of the expected lidar caused by the temporal spatial differences between OMPS and the OHP lidar. Then, we compare the average of the variations calculated throughout the study with the variation in the measurements obtained, and we can see that the calculated variations are between 2 and 3 stds of the measured variations.

#### 4.4. Discussion and Conclusion of Comparisons

The lidars chosen are positioned at different locations on the planet and have already validated numerous data sets, giving a very good idea of the quality of the OMPS temperature profiles obtained using our NSRTM. Despite the fact that it is difficult to estimate the differences caused by temporal spatial errors (gravity waves, atmospheric tides, etc.) precisely because of the lack of data, the difference in temperature measured by OMPS and lidars generally does not exceed 5 K along the profile, except in the case of MLO below 35 km and HOH above 70 km. As much as we know that in the case of HOH this is probably due to the fact that lidar rarely gives profiles above 70 km, and when they do it is with significant instrumental errors, in the case of MLO it is more complicated to explain these differences. For the moment, the lead that we favour is a higher aerosol content, but this needs to be studied further.

For models, ERA5 is a meteorological analysis combining a sophisticated atmospheric model and global observations. These temperature fields show excellent results in the stratosphere [25]. They are also in very good agreement with the OMPS data, down to 50 km ( $\sim 3$  K). In the mesosphere, on the other hand, the differences increase very quickly at all of the lidar sites, confirming the previous results with observations from the other lidar sites. The differences between the OMPS data and the MSIS climatological model show a high degree of consistency between the sites and are very similar to the differences with the lidars, with MSIS being a climatological model showing excellent results on average.

## 5. Application to a Miniaturised Instrument

### 5.1. Application to a Miniaturised Instrument

One of the aims of this study was also to test whether this method would be reliable enough for use on a smaller instrument such as a cubesat. The lack of temperature data in the mesosphere, the biases and drifts observed in the European Centre Model, and the



perturbation of atmospheric tides are driving the development of a nanosat constellation to study molecular diffusion [34]. Tests using GOMOS limb observations on ENVISAT have already demonstrated the benefits [32]. However, the complexity of measuring the GOMOS limb with a tracker that scans the limb seemed difficult to miniaturise. The method used in the OMPS instrument [41], by projecting the image of the entire limb onto a single CCD, seems more suitable, and the use of a dispersive element is not necessary and would further simplify a small instrument. This study, carried out with the OMPS instrument, has shown that it is possible to obtain excellent molecular scattering results with an OMPS-type instrument and in a simpler way than with GOMOS. The OMPS instrument can still be used to test the value of different wavelengths.

### 5.2. Aerosol Effects

Section 4.2 showed that attenuation on profiles below 330 nm does not allow temperature profiles to be obtained up to 30 km, so these wavelengths should be avoided.

Temperature profiles can be obtained from radiance profiles over the full range of solar irradiance in the visible and even in the near UV at a minimum starting altitude of 35 km. Below this altitude, molecular scattering is complemented by a contribution from aerosols suspended at these altitudes. As these effects are more significant at longer wavelengths, it seems preferable to use shorter wavelengths.

### 5.3. Noise Assessment

The 83 km limit in this study is not due to the method but to the limit of the measurement zone over which the OMPS electronics view the limb. As shown in Section 3.1, this configuration does not allow the noise level to be correctly estimated. The method used here shows that it is possible to eliminate the bias with the model, but ideally it is important to have a larger altitude range. This will correct all the measurement problems associated with noise. It should be noted, however, that the profiles least affected by this correction are the UV profiles, which shows that once again it seems preferable to use these wavelengths.

### 5.4. NO<sub>2</sub> and O<sub>3</sub> Corrections

The source of error associated with Rayleigh scattering is easily corrected using ERA5 profiles, which are very good when it starts to affect the results. Ozone absorption can be easily avoided by measuring the radiance between the Huggins and Chappuis absorption bands. The NO<sub>2</sub> correction remains stable throughout the usable spectral range and is therefore difficult to avoid. In order to minimise profile correction, it is therefore preferable to use the wavelengths where the overall attenuation of the signal is lowest, between the Huggins and Chappuis absorption bands.

## 6. Conclusions

Comparisons between OMPS, the lidars of the NDACC network and the MSIS and ERA5 models show that it is possible to obtain temperature profiles from instruments imaging the limb between 30 and 83 km with our NSRTM. We have seen that the median difference oscillates around 0 K with maximum peaks of 5 K. The variations in the measured deviations correspond to between 2 and 3 std of the calculated deviations, showing that the gravity wave and atmospheric tide phenomena that occur between OMPS and the lidars are well observed.

The study also made it possible to establish all the difficulties involved in a project to monitor temperature in the middle atmosphere using CCD measurements of radiance at the limb. Stray light and background noise that can produce errors of up to 150 K in the upper mesosphere need to be corrected either by extending the field of view beyond molecular diffusion, like 130 km, or by estimating them using a simulated profile. Aerosol pollution starts between 30 and 35 km altitude and intensifies as altitude decreases or wavelength increases. Finally, simple scattering and absorption by O<sub>3</sub> and NO<sub>2</sub> are factors to be taken into account when designing such a mission, as we have seen that they can

generate errors of up to 120 K. To avoid all these effects as much as possible, it is preferable to observe the limb between the Huggins and Chappuis bands of absorption.

In addition to the creation of a completely new database using OMPS data, covering the whole planet in an area that is very difficult to study (the middle atmosphere), our NSRTM is very easy to use and can be applied to any instrument that measures the radiance of the Earth's limb between 30 and 130 km in all visible and near-UV wavelengths, with better results near 340 nm to limit the effect of aerosols or 385 nm to limit the correction. As already demonstrated by the GOMOS instrument, this opens the door to the creation of a limb temperature database using existing and future instruments—for example, embedded in cubesats—drastically reducing the number of times we need to observe our planet with better time sampling by constellation on several successive orbits.

**Author Contributions:** Writing—original draft, P.D.C.L.; Writing—review & editing, P.K., A.H., M.M., G.J. and A.M. All authors have read and agreed to the published version of the manuscript.

**Funding:** This work benefited from State aid managed by the National Research Agency under France 2030 bearing the reference ANR-23-CMAS-0001.

**Data Availability Statement:** The original contributions presented in the study are included in the article, further inquiries can be directed to the corresponding author.

**Acknowledgments:** The lidar data used in this publication are publicly available as part of the Network for the Detection of Atmospheric Composition Change (NDACC) and are available through the NDACC international website, [www.ndacc.org](http://www.ndacc.org) (accessed on 12 October 2024), and through the French national centre for Atmospheric Data and Services, AERIS: [www.aeris-data.fr/projects/ndacc-france](http://www.aeris-data.fr/projects/ndacc-france) (accessed on 7 June 2024). Lidar operations are supported by CNRS, NASA, CNES, La Réunion and Versailles Saint-Quentin en Yvelines universities. This project was performed with the support of the Direction de l'Armement from the French Ministry of Armed Forces under the contract 202395002. The OMPS data used in this publication are freely accessible via the <https://www.earthdata.nasa.gov/> (accessed on 24 September 2024) website. We would also like to thank the MPI-Mainz UV/VIS Spectral Atlas of Gaseous Molecules, which provides a huge open-access data set of molecular absorption via the [www.uv-vis-spectral-atlas-mainz.org](http://www.uv-vis-spectral-atlas-mainz.org) (accessed on 3 July 2024) website. This study is part of the preparation of the ESA mission ALTIUS in collaboration with BIRA-IASB, with a funding contribution of the CNES.

**Conflicts of Interest:** The authors declare no conflict of interest.

## References

1. Tett, S.F.; Betts, R.; Crowley, T.J.; Gregory, J.; Johns, T.C.; Jones, A.; Osborn, T.J.; Öström, E.; Roberts, D.L.; Woodage, M.J. The impact of natural and anthropogenic forcings on climate and hydrology since 1550. *Clim. Dyn.* **2006**, *28*, 3–34. [\[CrossRef\]](#)
2. Beig, G.; Keckhut, P.; Lowe, R.P.; Roble, R.G.; Mlynarczyk, M.G.; Scheer, J.; Fomichev, V.I.; Offermann, D.; French, W.J.R.; Shepherd, M.G.; et al. Review of Mesospheric temperature Trends. *Rev. Geophys.* **2003**, *41*, 1015. [\[CrossRef\]](#)
3. Hauchecorne, A.; Keckhut, P.; Chanin, M. *Dynamics and Transport in the Middle Atmosphere Using Remote Sensing Techniques from Ground and Space*; Springer: Dordrecht, The Netherlands, 2009; pp. 665–683. [\[CrossRef\]](#)
4. Salby, M.L.; Callaghan, P.; Keckhut, P.; Godin, S.; Guirlet, M. Interannual changes of temperature and ozone: Relationship between the lower and upper stratosphere. *J. Geophys. Res.* **2002**, *107*, ACH 1-1–ACH 1-8. [\[CrossRef\]](#)
5. Rind, D.; Suozzo, R.; Balachandran, N.K.; Lacis, A.A.; Russell, G.L. The GISS Global Climate-Middle Atmosphere Model. Part I: Model Structure and Climatology. *J. Atmos. Spheric Sci.* **1988**, *45*, 329–370. [\[CrossRef\]](#)
6. Rind, D.; Suozzo, R.; Balachandran, N.K. The GISS Global Climate-Middle Atmosphere Model. Part II. Model variability due to interactions between planetary waves, the mean circulation and gravity wave drag. *J. Atmos. Sci.* **1988**, *45*, 371–386. [\[CrossRef\]](#)
7. Keckhut, P.; Randel, W.J.; Claud, C.; Leblanc, T.; Steinbrecht, W.; Funatsu, B.M.; Bencherif, H.; Mcdermid, I.S.; Hauchecorne, A.; Long, C.; et al. An evaluation of uncertainties in monitoring middle atmosphere temperatures with the ground-based LIDAR network in support of space observations. *J. Atmos. Sol.-Terr. Phys.* **2011**, *73*, 627–642. [\[CrossRef\]](#)
8. Maury, P.; Claud, C.; Manzini, E.; Hauchecorne, A.; Keckhut, P. Characteristics of stratospheric warming events during Northern winter. *Journal of geophysical research. Atmospheres* **2016**, *121*, 5368–5380. [\[CrossRef\]](#)
9. Mzé, N.; Hauchecorne, A.; Keckhut, P.; Thétis, M. Vertical distribution of gravity wave potential energy from long-term Rayleigh lidar data at a northern middle-latitude site. *Journal of geophysical research. Atmospheres* **2014**, *119*, 12069–12083. [\[CrossRef\]](#)
10. Ardalan, M.; Keckhut, P.; Hauchecorne, A.; Wing, R.; Meftah, M.; Farhani, G. Updated Climatology of Mesospheric Temperature Inversions Detected by Rayleigh Lidar above Observatoire de Haute Provence, France, Using a K-Mean Clustering Technique. *Atmosphere* **2022**, *13*, 814. [\[CrossRef\]](#)

11. Baldwin, M.P.; Dunkerton, T.J. Stratospheric harbingers of anomalous weather regimes. *Science* **2001**, *294*, 581–584. [\[CrossRef\]](#)
12. Shaw, T.A.; Perlwitz, J.; Weiner, O.M. Troposphere-Stratosphere coupling: Links to North Atlantic weather and climate, including their representation in CMIP5 models. *J. Geophys. Res. Atmos.* **2014**, *119*, 5480–5864. [\[CrossRef\]](#)
13. Charlton-Perez, A.; Ferranti, L.; Lee, R.W. The influence of the stratospheric state on North Atlantic weather regimes. *Q. J. R. Soc.* **2018**, *144*, 1140–1151. [\[CrossRef\]](#)
14. Mariaccia, A.; Keckhut, P.; Hauchecorne, A. Classification of stratosphere winter evolutions into four different scenarios in the Northern hemisphere. *J. Geophys. Res. Atmos.* **2022**, *127*, e2022JD036662. [\[CrossRef\]](#)
15. Mariaccia, A.; Keckhut, P.; Hauchecorne, A. Classification of stratosphere winter evolutions into four different scenarios in the Northern hemisphere: Part B coupling with the surface. *ESS Open Arch.* **2023**. [\[CrossRef\]](#)
16. Srivastava, N.; Mierla, M.; Zhang, J. Editorial: Space Weather Prediction: Challenges and Prospects. *Front. Astron. Space Sci.* **2021**, *8*, 230. [\[CrossRef\]](#)
17. Beagley, S.R.; McLandress, C.; Fomichev, V.I.; Ward, W.E. The extended Canadian Middle Atmosphere model. *Geophys. Res. Lett.* **2000**, *27*, 2529–2532. [\[CrossRef\]](#)
18. Baldwin, M.P.; Stephenson, D.B.; Thompson, D.W.J.; Dunkerton, T.J.; Charlton, A.J.; O'Neill, A. Stratospheric memory and skill of Extended-Range weather forecasts. *Science* **2003**, *301*, 636–640. [\[CrossRef\]](#) [\[PubMed\]](#)
19. Osprey, S.; Gray, L.J.; Hardiman, S.C.; Butchart, N.; Bushell, A.C.; Hinton, T. The climatology of the Middle Atmosphere in a vertically extended version of the Met Office's climate Model. Part I: Mean state. *J. Atmos. Sci.* **2010**, *67*, 1509–1525. [\[CrossRef\]](#)
20. Parker, D.E.; Cox, D.I. Towards a consistent global climatological rawinsonde data-base. *Int. J. Climatol.* **1995**, *15*, 473–496. [\[CrossRef\]](#)
21. Ladstädter, F.; Steiner, A.; Foelsche, U.; Haimberger, L.; Tavolato, C.; Kirchengast, G. An assessment of differences in lower stratospheric temperature records from (A)MSU, radiosondes, and GPS radio occultation. *Atmos. Meas. Tech.* **2011**, *4*, 1965–1977. [\[CrossRef\]](#)
22. Keckhut, P.; Schmidlin, F.; Hauchecorne, A.; Chanin, M. Stratospheric and mesospheric cooling trend estimates from u.s. rocketsondes at low latitude stations (8°S–34°N), taking into account instrumental changes and natural variability. *J. Atmos. Sol.-Terr. Phys.* **1999**, *61*, 447–459. [\[CrossRef\]](#)
23. Wing, R.; Hauchecorne, A.; Keckhut, P.; Godin-Beekmann, S.; Khaykin, S.; McCullough, E.M.; Mariscal, J.F.; d'Almeida, E. LIDAR Temperature Series in the Middle Atmosphere as a reference data set—Part 1: Improved retrievals and a 20-year cross-validation of two co-located French LIDARs. *Atmos. Meas. Tech.* **2018**, *11*, 5531–5547. [\[CrossRef\]](#)
24. Marlton, G.; Charlton-Perez, A.; Harrison, G.; Polichtchouk, I.; Hauchecorne, A.; Keckhut, P.; Wing, R.; Leblanc, T.; Steinbrecht, W. Using a network of temperature LIDARs to identify temperature biases in the upper stratosphere in ECMWF reanalyses. *Atmos. Chem. Phys.* **2021**, *21*, 6079–6092. [\[CrossRef\]](#)
25. Mariaccia, A.; Keckhut, P.; Hauchecorne, A.; Claud, C.; Le Pichon, A.; Meftah, M.; Khaykin, S. Assessment of ERA-5 temperature variability in the middle atmosphere using Rayleigh LIDAR measurements between 2005 and 2020. *Atmosphere* **2022**, *13*, 242. [\[CrossRef\]](#)
26. Hervig, M.E.; Russell, J.M.; Gordley, L.L.; Park, J.H.; Drayson, S.R.; Deshler, T. Validation of aerosol measurements from the halogen occultation experiment. *J. Geophys. Res.* **1996**, *101*, 10267–10275. [\[CrossRef\]](#)
27. Remsberg, E.E.; Bhatt, P.P.; Deaver, L.E. Seasonal and longer-term variations in middle atmosphere temperature from HALOE on UARS. *J. Geophys. Res.* **2002**, *107*, ACL 18-1–ACL 18-13. [\[CrossRef\]](#)
28. Hauchecorne, A.; Chanin, M. Density and temperature profiles obtained by LIDAR between 35 and 70 km. *Geophys. Res. Lett.* **1980**, *7*, 565–568. [\[CrossRef\]](#)
29. Clancy, R.T.; Rusch, D.W.; Callan, M. Temperature minima in the average thermal structure of the Middle Mesosphere (70–80 km) from analysis of 40- to 92-km SME global temperature profiles. *J. Geophys. Res.* **1994**, *99*, 19001–19020. [\[CrossRef\]](#)
30. Shepherd, M.G.; Reid, B.; Zhang, S.; Solheim, B.H.; Shepherd, G.G.; Wickwar, V.B.; Herron, J.P. Retrieval and validation of mesospheric temperatures from wind imaging interferometer observations. *J. Geophys. Res.* **2001**, *106*, 24813–24829. [\[CrossRef\]](#)
31. Sheese, P.E.; Strong, K.; Llewellyn, E.J.; Gattinger, R.L.; Russell, J.M., III; Boone, C.D.; Hervig, M.E.; Sica, R.J.; Bando, J. Assessment of the quality of OSIRIS mesospheric temperatures using satellite and ground-based measurements. *Atmos. Meas. Tech.* **2012**, *5*, 2993–3006. [\[CrossRef\]](#)
32. Hauchecorne, A.; Blanot, L.; Wing, R.; Keckhut, P.; Khaykin, S.; Bertaux, J.L.; Meftah, M.; Claud, C.; Sofieva, V. A new Mesospheric data set of temperature profiles from 35 to 85 km using Rayleigh scattering at limb from GOMOS/ENVISAT daytime observations. *Atmos. Meas. Tech.* **2019**, *12*, 749–761. [\[CrossRef\]](#)
33. Kyrölä, E.; Tamminen, J.; Leppelmeier, G.W.; Sofieva, V.; Hassinen, S.; Bertaux, J.L.; Hauchecorne, A.; Dalaudier, F.; Cot, C.; Korabely, O.; et al. GOMOS on Envisat: An overview. *Adv. Space Res.* **2004**, *33*, 1020–1028. [\[CrossRef\]](#)
34. Keckhut, P.; Hauchecorne, A.; Meftah, M.; Khaykin, S.; Claud, C.; Simoneau, P. Middle-Atmosphere temperature monitoring addressed with a constellation of CubeSats dedicated to climate issues. *J. Atmos. Ocean. Technol.* **2021**, *38*, 685–693. [\[CrossRef\]](#)
35. Meftah, M.; Clavier, C.; Sarkissian, A.; Hauchecorne, A.; Bekki, S.; Lefèvre, F.; Galopeau, P.; Dahoo, P.R.; Pazmino, A.; Vieau, A.J.; et al. Uvsq-Sat NG, a New CubeSat Pathfinder for Monitoring Earth Outgoing Energy and Greenhouse Gases. *Remote Sens.* **2023**, *15*, 4876. [\[CrossRef\]](#)
36. Chen, Z.; Schwartz, M.J.; Bhartia, P.K.; Schoeberl, M.; Kramarova, N.; Jaross, G.; DeLand, M. Mesospheric and Upper Stratospheric Temperatures From OMPS-LP. *Earth Space Sci.* **2023**, *10*, e2022EA002763. [\[CrossRef\]](#)

37. Singh, U.N.; Keckhut, P.; McGee, T.J.; Gross, M.R.; Hauchecorne, A.; Fishbein, E.F.; Waters, J.W.; Gille, J.C.; Roche, A.E.; Russell, J.M., III. Stratospheric temperature measurements by two collocated NDSC lidars during UARS validation campaign. *J. Geophys. Res.* **1996**, *101*, 10287–10297. [\[CrossRef\]](#)
38. Keckhut, P.; McDermid, S.; Swart, D.; McGee, T.; Godin-Beekmann, S.; Adriani, A.; Barnes, J.; Baray, J.L.; Bencherif, H.; Claude, H.; et al. Review of ozone and temperature lidar validations performed within the framework of the Network for the Detection of Stratospheric Change. *J. Environ. Monit.* **2004**, *6*, 721. [\[CrossRef\]](#) [\[PubMed\]](#)
39. Picone, J.M.; Hedin, A.E.; Drob, D.P.; Aikin, A.C. NRLMSISE-00 empirical model of the atmosphere: Statistical comparisons and scientific issues. *J. Geophys. Res.* **2002**, *107*, SIA 15-1–SIA 15-16. [\[CrossRef\]](#)
40. Bell, B.; Hersbach, H.; Simmons, A.; Berrisford, P.; Dahlgren, P.; Horányi, A.; Muñoz-Sabater, J.; Nicolas, J.; Radu, R.; Schepers, D.; et al. The ERA5 global reanalysis: Preliminary extension to 1950. *Q. J. R. Meteorol. Soc.* **2021**, *147*, 4186–4227. [\[CrossRef\]](#)
41. Jaross, G.; Bhartia, P.K.; Chen, G.; Kowitt, M.; Haken, M.; Chen, Z.; Xu, P.; Warner, J.; Kelly, T. OMPS Limb Profiler instrument performance assessment. *J. Geophys. Res. Atmos.* **2014**, *119*, 4399–4412. [\[CrossRef\]](#)
42. Kurylo, M.J. Network for the detection of stratospheric change. *Remote Sens. Atmos. Chem.* **1991**, *1491*, 168–174.
43. Fishbein, E.F.; Cofield, R.E.; Froidevaux, L.; Jarnot, R.F.; Lungu, T.; Read, W.G.; Shippony, Z.; Waters, J.W.; McDermid, I.S.; McGee, T.J.; et al. Validation of UARS Microwave Limb Sounder temperature and pressure measurements. *J. Geophys. Res. Atmos.* **1996**, *101*, 9983–10016. [\[CrossRef\]](#)
44. Gille, J.C.; Bailey, P.L.; Massie, S.T.; Lyjak, L.V.; Edwards, D.P.; Roche, A.E.; Kumer, J.B.; Mergenthaler, J.L.; Gross, M.R.; Hauchecorne, A.; et al. Accuracy and precision of cryogenic limb array etalon spectrometer (CLAES) temperature retrievals. *J. Geophys. Res.* **1996**, *101*, 9583–9601. [\[CrossRef\]](#)
45. Wu, D.L.; Read, W.G.; Shippony, Z.; Leblanc, T.; Duck, T.J.; Ortland, D.A.; Sica, R.J.; Argall, P.S.; Oberheide, J.; Hauchecorne, A.; et al. Mesospheric temperature from UARS MLS: Retrieval and validation. *J. Atmos. Sol.-Terr. Phys.* **2003**, *65*, 245–267. [\[CrossRef\]](#)
46. Ridolfi, M.; Blum, U.; Carli, B.; Catoire, V.; Ceccherini, S.; Claude, H.; De Clercq, C.; Fricke, K.H.; Friedl-Vallon, F.; Iarlori, M.; et al. Geophysical validation of temperature retrieved by the ESA processor from MIPAS/ENVISAT atmospheric limb-emission measurements. *Atmos. Chem. Phys.* **2007**, *7*, 4459–4487. [\[CrossRef\]](#)
47. Sica, R.J.; Izawa, M.R.M.; Walker, K.A.; Boone, C.; Petelina, S.V.; Argall, P.S.; Bernath, P.; Burns, G.B.; Catoire, V.; Collins, R.L.; et al. Validation of the Atmospheric Chemistry Experiment (ACE) version 2.2 temperature using ground-based and space-borne measurements. *Atmos. Chem. Phys.* **2008**, *8*, 35–62. [\[CrossRef\]](#)
48. Sivakumar, V.; Prasanth, V.P.; Kishore, P.; Bencherif, H.; Keckhut, P. Rayleigh LIDAR and satellite (HALOE, SABER, CHAMP and COSMIC) measurements of stratosphere-mesosphere temperature over a southern sub-tropical site, Reunion (20.8°S; 55.5°E): Climatology and comparison study. *Ann. Geophys.* **2011**, *29*, 649–662. [\[CrossRef\]](#)
49. Wing, R.; Hauchecorne, A.; Keckhut, P.; Godin-Beekmann, S.; Khaykin, S.; McCullough, E. LIDAR Temperature Series in the Middle Atmosphere as a reference data set—Part 2: Assessment of temperature observations from MLS/AURA and SABER/TIMED satellites. *Atmos. Meas. Tech.* **2018**, *11*, 6703–6717. [\[CrossRef\]](#)
50. Funatsu, B.M.; Claud, C.; Keckhut, P.; Hauchecorne, A. Cross-validation of Advanced Microwave Sounding Unit and lidar for long-term upper-stratospheric temperature monitoring. *J. Geophys. Res.* **2008**, *113*, D23108. [\[CrossRef\]](#)
51. Funatsu, B.M.; Claud, C.; Keckhut, P.; Hauchecorne, A.; Leblanc, T. Regional and seasonal stratospheric temperature trends in the last decade (2002–2014) from AMSU observations. *Atmospheres* **2016**, *121*, 8172–8185. [\[CrossRef\]](#)
52. Wing, R.; Steinbrecht, W.; Godin-Beekmann, S.; McGee, T.J.; Sullivan, J.T.; Sumnicht, G.; Ancellet, G.; Hauchecorne, A.; Khaykin, S.; Keckhut, P. Intercomparison and evaluation of ground- and satellite-based stratospheric ozone and temperature profiles above Observatoire de Haute-Provence during the Lidar Validation NDACC Experiment (LAVANDE). *Atmos. Meas. Tech.* **2020**, *13*, 5621–5642. [\[CrossRef\]](#)
53. Leblanc, T.; McDermid, I.S.; Hauchecorne, A.; Keckhut, P. Evaluation of optimization of lidar temperature analysis algorithms using simulated data. *J. Geophys. Res.* **1998**, *103*, 6177–6187. [\[CrossRef\]](#)
54. Wild, J.D.; Gelman, M.E.; Miller, A.J.; Chanin, M.L.; Hauchecorne, A.; Keckhut, P.; Farley, R.; Dao, P.D.; Meriwether, J.W.; Gobbi, G.P.; et al. Comparison of stratospheric temperatures from several lidars, using National Meteorological Center and microwave limb sounder data as transfer references. *J. Geophys. Res.* **1995**, *100*, 11105–11111. [\[CrossRef\]](#)
55. Emmert, J.T.; Drob, D.P.; Picone, J.M.; Siskind, D.E.; Jones, M., Jr.; Mlyneczek, M.G.; Bernath, P.F.; Chu, X.; Doornbos, E.; Funke, B.; et al. NRLMSIS 2.0: A Whole-Atmosphere Empirical Model of Temperature and Neutral Species Densities. *Earth Space Sci.* **2021**, *8*, e2020eaEA001321. [\[CrossRef\]](#)
56. Hersbach, H.; Bell, B.; Berrisford, P.; Hirahara, S.; Horányi, A.; Muñoz-Sabater, J.; Nicolas, J.; Peubey, C.; Radu, R.; Schepers, D.; et al. The ERA5 global reanalysis. *Q. J. R. Meteorol. Soc.* **2020**, *146*, 1999–2049. [\[CrossRef\]](#)
57. Keckhut, P.; Hauchecorne, A.; Chanin, M.L. A Critical Review of the Database Acquired for the Long-Term Surveillance of the Middle Atmosphere by the French Rayleigh Lidars. *J. Atmos. Ocean. Technol.* **1993**, *10*, 850–867. [\[CrossRef\]](#)
58. Khaykin, S.M.; Godin-Beekmann, S.; Keckhut, P.; Hauchecorne, A.; Jumelet, J.; Vernier, J.P.; Bourassa, A.; Degenstein, D.A.; Rieger, L.A.; Bingen, C.; et al. Variability and evolution of the midlatitude stratospheric aerosol budget from 22 years of ground-based lidar and satellite observations. *Atmos. Chem. Phys.* **2017**, *17*, 1829–1845. [\[CrossRef\]](#)
59. Bucholtz, A. Rayleigh-scattering calculations for the terrestrial atmosphere. *Appl. Opt.* **1995**, *34*, 2765. [\[CrossRef\]](#)
60. Serdyuchenko, A.; Gorshelev, V.; Weber, M.; Chehade, W.; Burrows, J.P. High spectral resolution ozone absorption cross-sections—Part 2: Temperature dependence. *Atmos. Meas. Tech.* **2014**, *7*, 625–636. [\[CrossRef\]](#)



61. Kramarova, N.A.; Bhartia, P.K.; Jaross, G.; Moy, L.; Xu, P.; Chen, Z.; DeLand, M.; Froidevaux, L.; Livesey, N.; Degenstein, D.; et al. Validation of ozone profile retrievals derived from the OMPS LP version 2.5 algorithm against correlative satellite measurements. *Atmos. Meas. Tech.* **2018**, *11*, 2837–2861. [[CrossRef](#)]
62. Bogumil, K.; Orphal, J.; Homann, T.; Voigt, S.; Spietz, P.; Fleischmann, O.C.; Vogel, A.; Hartmann, M.; Kromminga, H.; Bovensmann, H.; et al. Measurements of molecular absorption spectra with the SCIAMACHY pre-flight model: Instrument characterization and reference data for atmospheric remote-sensing in the 230–2380 nm region. *J. Photochem. Photobiol. A Chem.* **2003**, *157*, 167–184. [[CrossRef](#)]
63. Kyrölä, E.; Andersson, M.E.; Verronen, P.T.; Laine, M.; Tukiainen, S.; Marsh, D.R. Middle atmospheric ozone, nitrogen dioxide and nitrogen trioxide in 2002–2011: SD-WACCM simulations compared to GOMOS observations. *Atmos. Chem. Phys.* **2018**, *18*, 5001–5019. [[CrossRef](#)]
64. Meftah, M.; Sarkissian, A.; Keckhut, P.; Hauchecorne, A. The SOLAR-HRS New High-Resolution Solar Spectra for Disk-Integrated, Disk-Center, and Intermediate Cases. *Remote Sens.* **2023**, *15*, 3560. [[CrossRef](#)]

**Disclaimer/Publisher’s Note:** The statements, opinions and data contained in all publications are solely those of the individual author(s) and contributor(s) and not of MDPI and/or the editor(s). MDPI and/or the editor(s) disclaim responsibility for any injury to people or property resulting from any ideas, methods, instructions or products referred to in the content.